



HAL
open science

Computational solution for fluid flow under solid/liquid phase change conditions

Mohammed El Ganaoui, André Lamazouade, Patrick Bontoux, Dominique Morvan

► **To cite this version:**

Mohammed El Ganaoui, André Lamazouade, Patrick Bontoux, Dominique Morvan. Computational solution for fluid flow under solid/liquid phase change conditions. *Computers and Fluids*, 2002, 31 (4-7), pp.539-556. 10.1016/S0045-7930(01)00067-6 . hal-00838453

HAL Id: hal-00838453

<https://hal.science/hal-00838453>

Submitted on 16 Jan 2024

HAL is a multi-disciplinary open access archive for the deposit and dissemination of scientific research documents, whether they are published or not. The documents may come from teaching and research institutions in France or abroad, or from public or private research centers.

L'archive ouverte pluridisciplinaire **HAL**, est destinée au dépôt et à la diffusion de documents scientifiques de niveau recherche, publiés ou non, émanant des établissements d'enseignement et de recherche français ou étrangers, des laboratoires publics ou privés.

Computational solution for fluid flow under solid/liquid phase change conditions

M. El Ganaoui ^{a,*}, A. Lamazouade ^b, P. Bontoux ^b, D. Morvan ^b

^a *SPCTS UMR 6638 CNRS, Faculté des Sciences, 87000 Limoges, France*

^b *LMSNM FRE 2405, Université d'Aix-Marseille II, Marseille, France*

A fixed grid method based on an enthalpy–porosity formulation for liquid/solid phase transition is extended to compute the time-dependent solutal convection in the melt during directional solidification of alloys. A finite volumes approximation is used for uniform and refined grids with a second order Euler scheme. The ability of the method to describe accurately the flow transitions and regimes is considered with respect to the results of the linear theory of stability and of available spectral accurate calculation.

Keywords: Solid/liquid phase change; Finite volumes; Time-dependent convection

1. Introduction

Directional solidification problems involve two domains of the mechanics that were intensively studied with significant contributions of the numerical methods: the computational fluid dynamics (CFD) [1–3] and thermal solid mechanics [3,4]. Various CFD methods have contributed to a better understanding of complex structures in fluid flow. Accounting solid/liquid phase change with complex boundary conditions, the complexity has increased and specific CFD development are required. Recently CFD methods extended to liquid/solid phase change have known an important development in relevant fields of the modeling as physics, applied mathematics, engineering and other fields [5] and is of fundamental importance for crystal growers, geologists and meteorologists [6,7] etc.

* Corresponding author.

E-mail address: ganaoui@l3m.univ-mrs.fr (M. El Ganaoui).

The existence of moving interface between solid and liquid characterizes directional solidification. Each method of solution must determine the position and the shape of the phase change front compatible with the governing conservation equations in each phase. Front tracking approach deals with a weak formulation of these equations with tracking the interface, which induces remeshing of both domains at each time step [8]. This kind of method is not suitable to investigate solidification of alloys exhibiting usually a ‘mushy region’ rather than a sharp interface.

For heat problems, it is possible to obtain front fixing approach by making coordinates transformation or variables transformation in the governing equations [8]. For coordinate transformation, the resulting equations maintain the same variables in the conservative laws with additional source terms issued from the transformation [9]. Stefan or similar conditions at the interface will be imposed in the new coordinates.

The enthalpy method gives a front fixing approach for energy equation without introducing coordinates transformation. The interface position is recovered a posteriori [8] and a number of authors have extended this front fixing approach so as to include the convection phenomena within the two phases mushy region [10–12,17,27]. We have developed a time-dependent enthalpy–porosity formulation for directional solidification. The energy equation is formulated with the enthalpy variable accounting implicitly the thermal Stefan condition at the interface [15, 25,28].

The interaction between solid and liquid phases is modeled by a Darcian type force in the phase change area. The behavior of the melt is similar with the flow of an incompressible fluid in a porous medium. This force is proportional to the relative phase velocity. It corresponds to a damping force depending on the anisotropic permeability of the mushy zone. The permeability depends on the liquid fraction and on the size of solidification microstructures. An informative discussion of a new slant on the general approach of continuum mechanics needed to analyze the formation of mushy zone is given in Ref. [19]. The method is extended to the presence of species diffusion: the solutal Stefan condition which expresses the solute incorporation or rejection across the interface is taken into account implicitly in a species equation valid in all the domain [25, 29,30,35,36].

To solve numerically the obtained set of Navier–Stokes, energy and species equations, a second order finite volumes approximation is used for space discretization (in the case of uniform mesh) with a second order Euler scheme for time discretization [3,15,18]. A PISO algorithm is used for solving coupled equations.

For the applications the vertical gradient freezing (Bridgman technique) for directional solidification is studied. The material is loaded into an ampoule, melted and solidified by varying the vertical field with a given translation. Convection in this system is driven by buoyancy differences induced by radial and axial temperatures and solute gradients. Regarding to the magnitude of the gradients, the geometry and the ampoule orientation with respect to the gravity direction, the convection can be steady or time dependent [15,21,24,26].

The thermal convection occurring in such systems studied in Refs. [15,28] shows that the enthalpy–porosity formulation in association with the finite volumes approximation simulate accurately complex flow pattern and heat transfer. Comparisons with spectral results in fluid phase only and finite element calculations in the two phases are achieved [15]. When the melt is below the crystal, the thermal gradient has a destabilizing effect and time-dependent convection develops to interact with melt/solid interface [15,28,34].

This study focuses on the occurrence of solutal convection in gradient freezing applications. Firstly, only the fluid phase is investigated and the results are validated with respect to spectral ones [13] then the full solid/liquid model is investigated. A linear approximation of the equilibrium phase diagram is considered for establishing relations between mass fraction and temperature fields to close the set of conservation equations [11,36].

2. Modeling

We consider a domain $D \subset \mathbb{R}^3$ under phase change transformation. The solid and liquid phases occupy respectively the domains D_s and D_l . The solid/liquid transition is assumed to occur in a small region I_{sl} . The governing equations for mass, momentum energy and species conservation must be taken into account for this situation through the interface in I_{sl} .

$\mathbf{x}(x, y, z)$ denotes the current point of D and $\mathbf{u}(u_x, u_y, u_z)$ the 3D velocity vector. T is the temperature and C the mass fraction. Liquid, solid and transition area are distinguished by using the suffixes l, s and sl respectively.

Reduced domain for space and time is obtained by choosing a reference length l_r and reference time t_r . Very different length scales are defined due to the characteristics time between thermal and solutal properties. A reference magnitude velocity is deduced by $u_r = l_r/t_r$. A thermal variation ΔT and a mass fraction variation ΔC respectively for thermal and solutal fields are chosen. The same notations for reduced variables are maintained. We introduce a liquid fraction f_l verifying:

$$\begin{aligned} f_l(\mathbf{x}, t) &= 0 & \text{if } \mathbf{x} \in D_s \\ 0 < f_l(\mathbf{x}, t) < 1 & \text{if } \mathbf{x} \in I_{sl} \\ f_l(\mathbf{x}, t) &= 1 & \text{if } \mathbf{x} \in D_l \end{aligned} \quad (1)$$

Introducing the reduced enthalpy variable for the energy equation:

$$h(\mathbf{x}, t) = T(\mathbf{x}, t) + f_l(x, t)Ste^{-1} \quad (2)$$

where $Ste = c\Delta T/L_f$ is the Stefan number: ratio between the sensible heat $c\Delta T$ and the latent heat of solidification L_f . Assuming constant and equal physical properties in the two phases (density, thermal conductivity and heat capacity) the energy equation has the following form:

$$\frac{\partial T}{\partial t} + \mathbf{u} \cdot \nabla T - [\alpha t_r/l_r^2]\Delta T + Ste^{-1} \frac{df_l}{dt} = 0 \quad (3)$$

the term $\alpha t_r/l_r^2$ is equal to unity for thermal time scaling ($t_r = l_r^2/\alpha$), gives Lewis number ($Le = \alpha/\mathcal{D}_1$) for solutal scaling ($t_r = l_r^2/\mathcal{D}_1$) and gives Prandtl number ($Pr = \alpha/\nu$) for dynamic scaling ($t_r = l_r^2/\nu$). If Ste^{-1} goes to 0 ($L_f = 0$), Eq. (3) goes to the classical one phase energy equation. In the case of pure substance solidified during a time duration τ , the transition area verify:

$$I_{sl} = \{(\mathbf{x}, t) \in D \times [0, \tau] / 0 < f_l(\mathbf{x}, t) < 1\} = \{(\mathbf{x}, t) \in D \times [0, \tau] / T_{sl}^- \leq T(\mathbf{x}, t) \leq T_{sl}^+\} \quad (4)$$

The difference $2\varepsilon(x, t) = T_{sl}^+ - T_{sl}^-$ characterizes the thermal thickness of the transition area and $f_l(x, t)$ is defined as:

$$f_1(x, t) = \frac{T - T_{sl}^-}{2\varepsilon(x, t)} \quad (5)$$

Note that the energy equation is valid in all the domain D and there is no need to write explicitly the thermal Stefan condition at the interface:

$$\frac{\partial T_l}{\partial \mathbf{n}} - \frac{\partial T_s}{\partial \mathbf{n}} = Ste^{-1} l_r \alpha^{-1} \mathbf{v} \cdot \mathbf{n} \quad (6)$$

where \mathbf{n} is the outer normal vector. The group $l_r \mathbf{v} \cdot \mathbf{n} / \alpha = \mathbf{v} \cdot \mathbf{n} / (\alpha / l_r)$ gives thermal Peclet number if the growth velocity is assumed equal to the normal velocity of the interface.

For the solidification of alloy the rejection or incorporation of the solute is given by a similar relation to the thermal Stefan condition at the interface [8]. To remove the need of writing this condition explicitly an average mass fraction is considered [11,17]:

$$C = f_1 C_1 + (1 - f_1) C_s \quad (7)$$

using the partition ratio $C_s / C_1 = k$ and neglecting the solute diffusion in the solid phase ($\partial C_s(x, t) / \partial t = 0$) the equation of the solute conservation is written [11,30]:

$$\frac{\partial C_1}{\partial t} + \mathbf{u} \cdot \nabla C_1 - [\mathcal{D}_1 t_r / l_r^2] \Delta C_1 + \left(\frac{\partial f_1}{\partial t} (1 - k) C_1 + (f_1 - 1) \frac{\partial C_1}{\partial t} \right) = 0 \quad (8)$$

the quantity $\mathcal{D}_1 t_r / l_r^2$ mentioning the solute diffusion in liquid phase is a dimensionless number equal to unity for solutal scale, gives the inverse of the Lewis number ($Le = \alpha / \mathcal{D}_1$) for the thermal scale and the inverse of the Schmidt number ($Sc = \nu / \mathcal{D}_1$) for problems reduced by dynamic time. The phase change occurs during the temperature interval given by the solidus and liquidus lines [11]. The linearized phase diagram gives:

$$T_{sol}^+ = T_{sol}(0) + \lambda C_{sl} \quad \text{and} \quad T_{sol}^- = T_{sol}(0) + \frac{\lambda}{k} C_{sl}$$

where $T_{sol}(0)$ is the melting temperature for pure solvent and λ is the slope of the liquidus. In this case the mushy zone is introduced by an ε depending on the phase diagram:

$$2\varepsilon(x, t) = \lambda \left(1 - \frac{1}{k} \right) C_{sl} \quad (9)$$

For the momentum equation a permeability term is introduced:

$$K(x, t) = \begin{cases} K_l \rightarrow +\infty & \text{if } x \in D_l \\ K_{sl} & \text{if } x \in I_{sl} \\ K_s \rightarrow 0 & \text{if } x \in D_s \end{cases} \quad (10)$$

The momentum equations takes the following form:

$$\frac{\partial \mathbf{u}}{\partial t} + \mathbf{u} \cdot \nabla \mathbf{u} + \nabla P - [\nu t_r / l_r^2] \Delta \mathbf{u} + (A_s C - A_t T) \hat{\mathbf{g}} + [t_r] K^{-1} \mathbf{u} = 0 \quad (11)$$

where the quantities $A_t = g \beta_t \Delta T t_r^2 / l_r$ and $A_s = g \beta_c \Delta C t_r^2 / l_r$ are dimensionless numbers giving for example thermal and solutal Grashof numbers respectively when we use a dynamic scale ($t_r = l_r^2 / \nu$), $\hat{\mathbf{g}}$ the unit gravity vector. Note that this equation contains asymptotically the behavior of the velocity in each media. When $K = K_l$, the term $K(x, t)^{-1} \mathbf{u}$ tends to zero and in the fluid domain D_l

and we solve a close approximation of the Navier–Stokes equations. When $K = K_s$, the term $K(x, t)^{-1} \mathbf{u}$ penalizes the momentum equation, the other terms of the equation become negligible and implies $\mathbf{u}_s \approx 0$. A theoretical justification is given by using a formulation by fictitious domain to study incompressible viscous flow inside fluid–porous-solid systems by using the Brinkman model in Refs. [22,23]. Eqs. (3), (8) and (11) must be coupled to the continuity equation:

$$\nabla \cdot \mathbf{u} = 0 \quad (12)$$

3. Numerical method

3.1. Finite volumes approximation

To explain the approach we consider the two-dimensional (2D) convection diffusion equation for a general variable φ with the velocity field in cartesian coordinates \mathbf{u} :

$$\frac{\partial \varphi}{\partial t} + \text{div}(\mathbf{F}(\varphi)) = f \quad (13)$$

$$\nabla \cdot \mathbf{u} = 0$$

$\mathbf{F}(\varphi) = \mathbf{u}\varphi - \gamma_\varphi \text{grad } \varphi$ is the advection–diffusion tensor of φ with the convective part $\mathbf{F}^c = \mathbf{u}\varphi$ and the diffusive part $\mathbf{F}^d = -\gamma_\varphi \text{grad } \varphi$.

Eq. (13) gives the expression of the conservation of φ in an infinitesimal domain, it is equivalent to write in any subdomain V and for all times t and t' :

$$\int_V \varphi(\mathbf{x}, t') \, d\mathbf{x} - \int_V \varphi(\mathbf{x}, t) \, d\mathbf{x} + \int_t^{t'} \int_{\partial V} \mathbf{F} \cdot \boldsymbol{\tau}_V(\mathbf{x}) \, d\sigma(\mathbf{x}) \, dt = \int_V \int_t^{t'} f(\mathbf{x}, \mathbf{t}) \, d\mathbf{x} \, dt \quad (14)$$

where $\boldsymbol{\tau}_V(\mathbf{x})$ is the normal vector to the boundary ∂V at point \mathbf{x} , outward to V .

In order to define a finite volumes scheme, the time derivative is approximated by a finite differences scheme on an increasing sequences on time $(t_n)_{n \in \mathbb{N}}$ with $t_0 = 0$. An ‘admissible’ mesh (see Ref. [18]) of the physical domain Ω of \mathbb{R}^2 is introduced and noted \mathcal{M} ($\Omega = \cup V, V \in \mathcal{M}$). The discrete unknowns at time $t_n = n \delta t$ (δt is the time step), are expected to be an approximation of φ on the cell V around the point $M_{i,j}$ and noted $\varphi_{i,j}^n$.

Eq. (13) is integrated over each cell V using the Gauss divergence theorem:

$$\int_V \left(\frac{\partial \varphi}{\partial t} \right)^n \, d\mathbf{x} + \int_{\partial V} \mathbf{F}^n \cdot \boldsymbol{\tau}_V \, d\sigma(\mathbf{x}) = \int_V f(\mathbf{x}, t_n) \, d\mathbf{x} \quad (15)$$

where $(\partial \varphi / \partial t)^n$ is given by the time scheme at the time step $t_n = n \delta t$ in the control volume V . The next step of the method is the approximation of the convective part $\mathbf{F}^c \cdot \boldsymbol{\tau}_V$ and the diffusive part $\mathbf{F}^d \cdot \boldsymbol{\tau}_V$ of the projected flux $\mathbf{F} \cdot \boldsymbol{\tau}_V$ over the boundary ∂V of each control volume.

3.1.1. Time discretization

The time integration is performed implicitly by using a three levels scheme, giving a second order truncation error in time.

$$\left(\frac{\partial \varphi}{\partial t}\right)^n = \frac{3\varphi^{n+2} - 4\varphi^{n+1} + \varphi^n}{2\delta t} + \mathcal{O}(\delta t^2) \quad (16)$$

3.1.2. Flux approximations

The diffusive part of the flux is discretized with a second order truncation error in space for uniform mesh:

$$\mathcal{F}_{i+1/2}^d = -\gamma_\varphi \frac{\varphi_{i+1,j} - \varphi_{i,j}}{x_{i+1} - x_i} + \mathcal{O}(\delta x^2)$$

Different discretizations for the convective fluxes are possible, central schemes apply a symmetric interpolation for $\varphi_{i+1/2}$. Upwind schemes apply a one side interpolation. Leonard and Mokhtari [33] has introduced QUICK and other schemes as a combination between the two kinds of interpolation. We have used QUICK scheme with a second order truncature in space. We write $\mathbf{F}_{i+1/2,j}^c = u_{i+1/2,j} \varphi_{i+1/2,j}$ where $\varphi_{i+1/2,j}$ is an approximation of φ at the east side of the volume V :

$$\varphi_{i+1/2,j} = \alpha \varphi_{i-3m,j} + \beta \varphi_{i-m,j} + \gamma \varphi_{i+m,j} \quad (17)$$

the subscript m is equal to 0 for $u_{i+1/2,j} > 0$ and -1 for $u_{i+1/2,j} < 0$. α , β and γ depends on $(x_{i-1}, x_i, x_{i+1/2})$ and x_{i+1} :

$$\alpha = \frac{(x_{i+1/2} - x_i)(x_{i+1/2} - x_{i+1})}{(x_{i-1} - x_i)(x_{i-1} - x_{i+1})}; \quad \beta = \frac{(x_{i+1/2} - x_{i-1})(x_{i+1/2} - x_{i+1})}{(x_i - x_{i-1})(x_i - x_{i+1})}$$

and

$$\gamma = \frac{(x_{i+1/2} - x_{i-1})(x_{i+1/2} - x_i)}{(x_{i+1} - x_{i-1})(x_{i+1} - x_{i-1})}$$

for uniform grid (α, β, γ) corresponds to $(-1/8, 6/8, 3/8)$.

4. Numerical simulations

4.1. Fluid model for solutal convection

4.1.1. Test case definition

To validate the finite volumes code, we consider available results for a test case using time-dependent approach with a high accuracy spectral methods [13,14]. The referred study describes various cycles of hysteresis connecting the different branches of the stable steady solution. The considered configuration is a 2D rectangular cavity restricted to fluid phase, the effects of front deformation are neglected in order to focus this study on the dynamic flow patterns induced by solutal convection. The concerned binary alloy Pb-30%Tl is characterized by $k = 1.1$, $Pr = 2.25 \times 10^{-2}$, $Le = 5400$ and $Sc = 121.5$. The solutal length $l_r = l_s = \mathcal{D}_1/u_p$ is used as a reference for space and $t_r = u_p^2/\mathcal{D}_1$ as a reference time. $\Delta C = C_\infty(k-1)/k$ is the reference mass fraction reject of Tl mass fraction at the solid/liquid interface corresponding to the diffusive solution [16]. C_∞ is the Tl mass fraction far from the interface. The control parameter used in the reference results is the solutal Rayleigh number:

$$Ra_s = Gr_s/Sc = \frac{g\beta_c \Delta C l_s^3}{\nu \mathcal{D}_1} = \frac{g\beta_c C_\infty (k-1) l_s^3}{k\nu \mathcal{D}_1} \quad (18)$$

According to that and to the absence of phase change, the set (12), (11) and (8) is written in the reduced domain $\{(x, y, t)/0 \leq x \leq A_x, 0 \leq y \leq A_y, 0 \leq t \leq \tau\}$:

$$\nabla \cdot \mathbf{u} = 0 \quad (19)$$

$$\frac{\partial \mathbf{u}}{\partial t} + \mathbf{u} \cdot \nabla \mathbf{u} - Sc \Delta \mathbf{u} + \nabla P - Gr_s C \hat{\mathbf{g}} = 0 \quad (20)$$

$$\frac{\partial C}{\partial t} + \mathbf{u} \cdot \nabla C = \Delta C \quad (21)$$

with boundary conditions.

For the reduced velocity (set to the opposite growth velocity), homogeneous Dirichlet conditions are imposed on the contour (Γ) for u_x and u_y as:

$$u_x|_\Gamma = 0 \quad (22)$$

$$u_y|_\Gamma = -1 \quad (23)$$

For the mass fraction field a Dirichlet condition is imposed at the top, homogeneous Neumann conditions on the vertical side, and a Robin condition at the bottom of the cavity to model the solute rejection rate into the fluid:

$$C(x, A_y, t) = (k-1)/k \quad (24)$$

$$\frac{\partial C(0, y, t)}{\partial x} = \frac{\partial C(A_x, y, t)}{\partial x} = 0 \quad (25)$$

$$\frac{\partial C(x, 0, t)}{\partial y} + (1-k)C(x, 0, t) = 0 \quad (26)$$

4.1.2. Finite volumes solution and comparison with spectral results

The investigated case corresponds to a reduced width $A_x = 9$ for a reduced height $A_y = 16$. With these dimensions, the problem is assumed free of confinement effects [13]. The simulation was carried out for solutal Rayleigh number $Ra_s \in [10, 100]$ covering modes from the steady diffusive solution to time-dependent one.

Chebyshev spectral or pseudo-spectral methods ensure important refinement near boundary layers that usually corresponds to the smallest characteristic length scale [2,20,21]. To compare our code with spectral one, uniform and refined grid are considered. Grid is refined around the bottom of the domain where mass fraction gradients are localized. In the horizontal direction 40 points of grid are used. In order to better describe the viscous boundary layer where are localized strong gradients of velocity a space step in geometrical progress is used with ratio $\delta x_i/\delta x_{i+1} = q > 1$. In the vertical direction, the accuracy of the solution is conditioned by the solute gradients calculation near the bottom of the domain. We choose to refine vertically the part

$[0, A_y/4]$ also. The steady solution of the Eq. (21) according to the boundary condition (23) gives an analytical solution of the mass fraction field:

$$C(y) = C_\infty \left(1 - \frac{k-1}{k} \exp(-y) \right) \quad (27)$$

The analytical solution shows the existence of an unit exponential diffusion layer adjacent to the interface to justify the choice of solutal length as a reference scale of space. The solute field decays from C_∞ far from the interface ($y \rightarrow \infty$) to ($C_\infty/k = C(0)$) near the interface.

The spectral code uses a space resolution corresponding to a Chebychev collocation method. The solutions were calculated by taking 45 points of Gauss–Lobatto in each space direction [13]. This reference solution has been compared to four cases of finite volumes discretization. The results are given grouped in Table 1 for $Ra_s = 35$. Qualitatively the solution (Fig. 1) shows the development of a convective cell for all the considered cases. From a quantitative point of view a good agreement is obtained for all calculations between the finite volume solutions and the spectral ones. The maximum difference corresponds for the uniform grid ($q = 1$): 3.6% for stream function and 2.2% for the mass-fraction field. The case defined in the second row of the Table 1 with $q = 1.07$ appears to give a good compromise between the time step and the grid definition.

To evaluate the theoretical threshold of solutal convection, linear stability analysis has been achieved by Gu erin et al. [16] for a large range of A_x considering a semi-infinite medium in the vertical direction and for both alloy systems ($k = 0.3$ and $k = 1.1$). Two general features are exhibited due to lateral confinement: a stabilizing effect on convection and a succession of odd and even convective critical modes. For the value $A_x = 9$ considered in our validation, the analysis predicts a competition between the even and odd modes of the convection. However, for aspect ratios $A_x < 10$, mode 1 corresponds to a mono-cellular asymmetrical and unstable mode. McFadden et al. [31] exhibited the subcritical nature of the bifurcation node coll for convective mono-cellular configurations. This bifurcation was then characterized by Impey et al. using a continuation method [32]. The bifurcation has always a bounded amplitude, but the change of stability occurs in a point noted Ra_1 lower than the threshold of first instability apparition Ra_2 . Varying the parameter of control Ra , we can follow an hysteresis cycle.

For present simulation the control parameter is the solutal Rayleigh number (Ra_s), the linear analysis gives $(Ra_s)_1 = 20.38$ and $(Ra_s)_2 = 15.25$ [14]. We have considered a range of $Ra_s \in [0, 100]$. Starting with the diffusive solution $Ra_s = 0$, the other ones are obtained successively for higher Ra_s (see Table 2).

Table 1

Solutions for four kinds of finite volumes grid and a reference spectral grid for $Ra_s = 35$. Maximum of stream-function ψ_{\max} and minimum of interface mass function $C_{sl \min}$ are compared

Method	Grid type	Time step	ψ_{\max}	$C_{sl \min}$
Finite volumes	Refined $q = 1.07$	5×10^{-2}	13.632	9.752
Finite volumes	Refined $q = 1.03$	5×10^{-3}	13.624	9.718
Finite volumes	Refined $q = 1.01$	4×10^{-4}	13.618	9.693
Finite volumes	Uniform $q = 1$ (40×105)	10^{-4}	14.112	9.906
Spectral	Collocation Chebychev (45×45)	10^{-4}	13.619	9.696

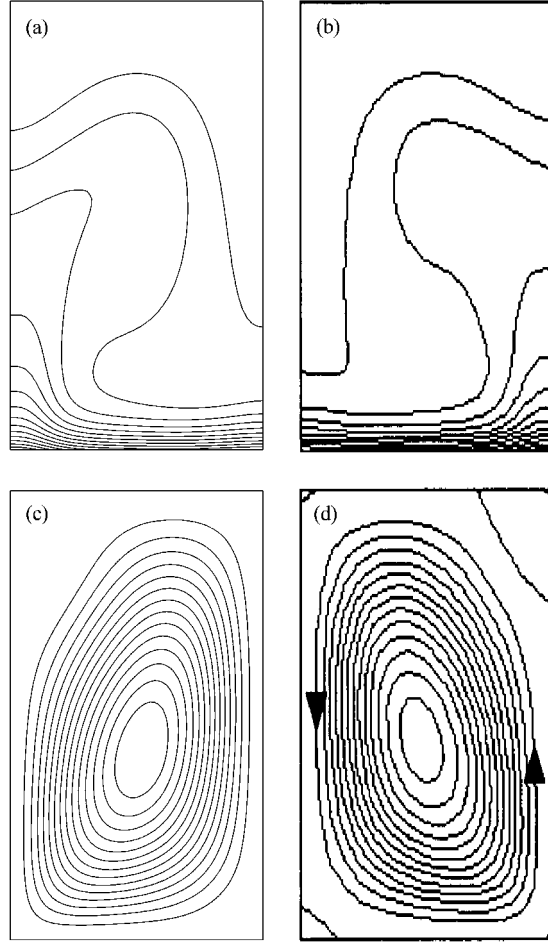


Fig. 1. Mass fraction configuration for: (a) Finite volumes and (b) spectral results. Dynamic configurations for: (c) finite volumes and (d) spectral results corresponding to $Ra_s = 35$. The orientation of the convective cells in both direct and indirect direction is equiprobable.

Table 2

Comparison of finite volumes and spectral results: transitions for $Ra_s \in [10, 60]$; $m = 1$ for one cellular flow, and $m = 2$ for two cellular flow. For steady solution the maximum of stream-function ψ_{\max} are compared. For periodic regime the frequencies f are compared

Ra_s	Finite volumes	Spectral
10	Steady diffusive $\psi_{\max} = 3.93 \times 10^{-3}$	Steady diffusive $\psi_{\max} = 1 \times 10^{-7}$
20	Steady $m = 1$; $\psi_{\max} = 8.58$	Steady $m = 1$; $\psi_{\max} = 8.91$
35	Steady $m = 1$; $\psi_{\max} = 13.63$	Steady $m = 1$; $\psi_{\max} = 13.619$
41	Periodic $m = 2$; $f = 0.105$	Periodic $m = 2$; $f = 0.110$
60	Periodic $m = 2$; $f = 0.177$	Periodic $m = 2$; $f = 0.192$

Obtained diffusive solution for $Ra_s = 10$ corresponds the analytical equation (27) and allows that the simulation takes into account correctly the Robin boundary condition imposed at the bottom of the domain. Below the critical threshold, the diffusive mode is obtained (for example $Ra_s = 20$). The isolines of mass fraction remain quasi-planar and the interfacial field remains constant. The signal of velocity diminishes slowly with the influence of solutal diffusion.

To reach high Ra values, the numerical simulation requires higher CPU time. The theory does not take into account the effects of the numerical diffusion. Taking as initial conditions a destabilized velocity field, a development of a mono-cellular convective mode for the threshold $Ra_s = 20$ is observed. The movement is ascending along the east wall and descending along the west wall as show it the isovalues of the mass fraction (Fig. 2). For $Ra_s = 41$ a second contrarotative cell appears in the top of the cavity (Fig. 3(a)). The regime becomes periodic with two cells in competition corresponding to the frequency $f = 0.105$. Fig. 4 shows three streamlines patterns at three stages for the periodic flow ($f = 0.177$) for $Ra_s = 60$ illustrating the transition between symmetric and asymmetric convection during time-dependent regime. The symmetry breaking of the solute field is also illustrated in Fig. 5. The dynamic configuration is similar to observed situations during Ga–Ge growth investigated in 2D cavity [15], the considered configuration in that case takes into account the solid/liquid interface interacting with the two cells particularly in the case of time-dependent melt.

4.2. Solidliquid model for solutal convection

A full model of Pb–30%Ti including solid and liquid phases is considered in an ampoule with aspect ratio $A = 20/9$. To focus the study on solutal influence, latent heat effects are neglected. The displacement of the ampoule is done at constant speed u_p . The reduced linear thermal

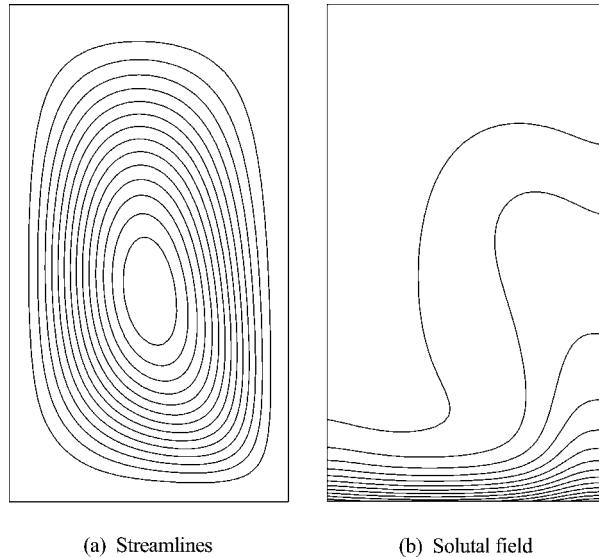


Fig. 2. Finite volumes results: monocellular regime illustrating the study solution for $Ra_s = 20$.

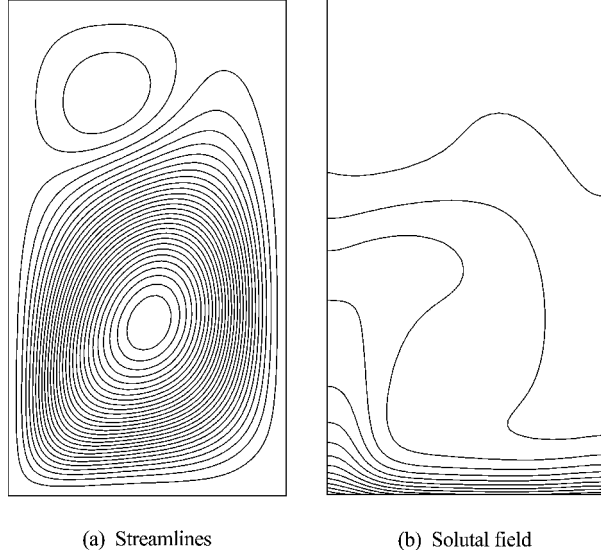


Fig. 3. Time-dependent regime for $Ra_s = 41$ illustrated with periodic solution corresponding to frequency $f = 0.105$.

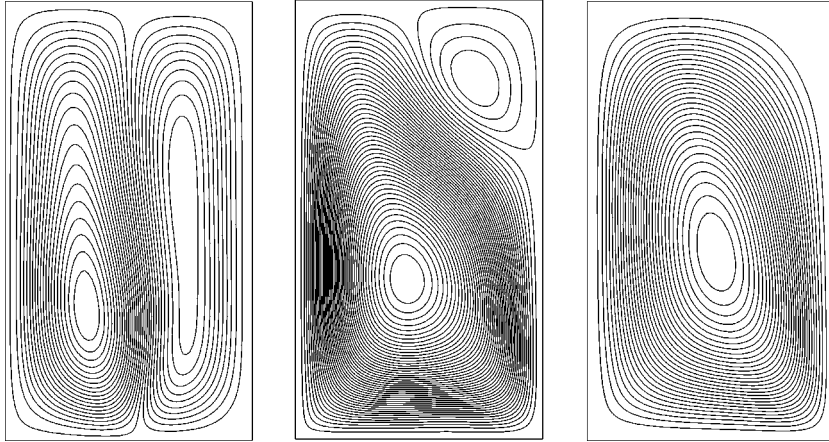


Fig. 4. Dynamic field for periodic solution corresponding to $Ra_s = 60$ ($f = 0.177$). Three configurations illustrating the transition between two-cellular and mono-cellular flow.

gradient is $G = 1/9$. We deduce approximately the reduced size of the mushy zone $\delta y_{\text{mushy}} = 0.818$. Homogeneous Dirichlet conditions are imposed for the velocity:

$$u_x|_{\Gamma} = u_y|_{\Gamma} = 0 \quad (28)$$

no permeable conditions implies a Neumann condition for the Thallium mass fraction field:

$$\frac{\partial C}{\partial n} \Big|_{\Gamma} = 0 \quad (29)$$

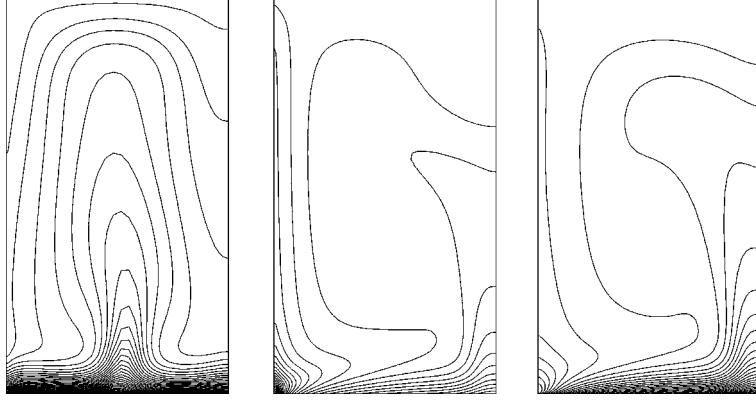


Fig. 5. Mass fraction field for periodic solution corresponding to $Ra_s = 60$ ($f = 0.177$). Three configurations illustrating the symmetry breaking.

for the thermal field a moving boundary conditions are applied to the adiabatic zone delimited by a cold point $y_c(t)$ and a hot point $y_h(t)$.

$$T(0, y, t) = T(A_x, y, t) = 0 \quad \text{for } y \leq y_c(t) \quad (30)$$

$$\frac{\partial T(0, y, t)}{\partial n} = \frac{\partial T(A_x, y, t)}{\partial n} = 0 \quad \text{for } y_c \leq y \leq y_h \quad (31)$$

$$T(0, y, t) = T(A_x, y, t) = 1 \quad \text{for } y \geq y_h(t) \quad (32)$$

the adiabatic zone moves at the solidification velocity u_p . The initial conditions correspond to an uniform mass fraction field of thallium $C(x, y, 0) = 0.3\%$ and an uniform thermal and dynamic fields $T(x, y, 0) = 0$; $\mathbf{u}(x, y, 0) = \mathbf{0}$.

A 40×140 grid is used. The space step in the horizontal direction is variable to refine the mesh near the walls. In the vertical direction the grid is uniform with a small step $\delta y_1 = 12.8 \times 10^{-2}$ to obtain a good representation for the phase change area (six space mesh in the mushy region). We use a time step $\delta t = 10^{-4}$ giving a correct time representation for the phase change phenomena under similar conditions as studied in Ref. [15]. We present here solutal results corresponding $Ra_s \in [10, 80]$, without taking into account the thermal convection $Ra_t = 0$. In order to examine coupled thermal and solutal convection, a configuration for $Ra_s = 20$ and $Ra_t = 500$ has been considered. The thermal field (Fig. 6) is not influenced by the convection in the melt, and it is independent on the Rayleigh number value. Figs. 7–9 show the mass fraction isovalues for respectively $Ra_s = 10$ (diffusive regime) to high $Ra_s = 80$. Successive solidification interfaces are represented in the Fig. 6. At the first steps the influence of initial condition is observed before a steady state with the same behavior of dynamic and thermal fields. This influence is shown also by considering vertical positions $z = z_i$ of the ampoule for diffusive regime ($Ra_s = 10$) at the first step and at the last step of the considered duration of growth (Fig. 10).

For the alloy solidification the relation (4) quantifies the coupling between the liquids isotherm and the solidification interface: $|T_{\text{sol}} - T_{\text{sol}}(0)| \leq |\lambda C_{\text{sl}}| = 1.1\%$. The phase diagram indicates that a

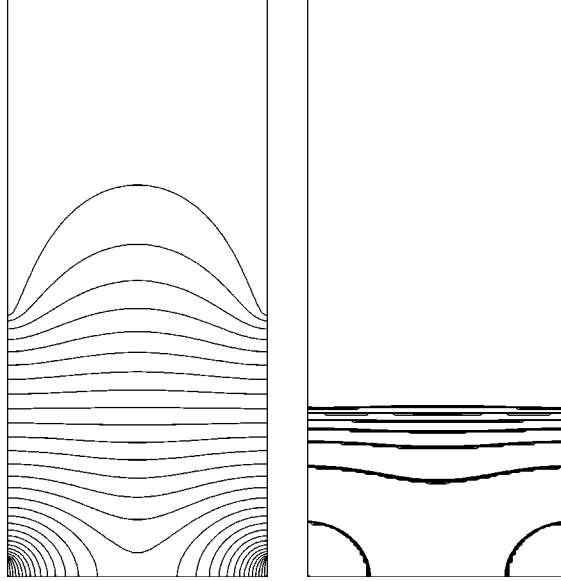


Fig. 6. Temperature field (left) and successive solidification interfaces (right) for the studied steps: these configurations are similar for all studied Ra_s , $0 \leq Ra_s \leq 100$.

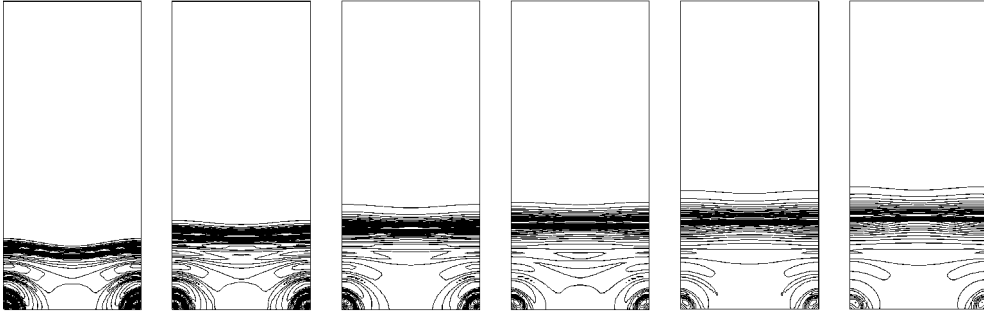


Fig. 7. Evolution of the mass fraction field for successive steps of growth, $Ra_s = 10$.

local variation of 10% of the field of mass fraction brings the variation on the thermal field, the thermal gradient in the zone of phase change is $G = 1/9$ to predict a small variation (1.1%) of the interface position around the liquidus curve.

The simulation carried out without taking into account the thermal convection gives similar dynamic mode in the melt. Figs. 11–13 show an axi-symmetrical convective hydrodynamic mode with two counter-rotating cells. The external contours of the cells approach tangentially the contour of the interface (Fig. 13). This fact explains the low perturbation in the mass fraction field structure (Figs. 7–9). All simulations give steady hydrodynamic regime. It is pointed out that the simulations given in Section 4.1 with modeling the segregation by a Robin's boundary condition favour the appearance of time-dependent structures is for lower value of the solutal Rayleigh

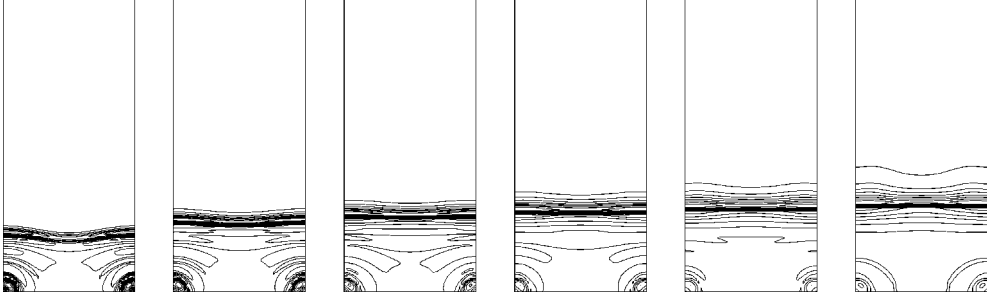


Fig. 8. Evolution of the mass fraction field for successive steps of growth, $Ra_s = 20$.

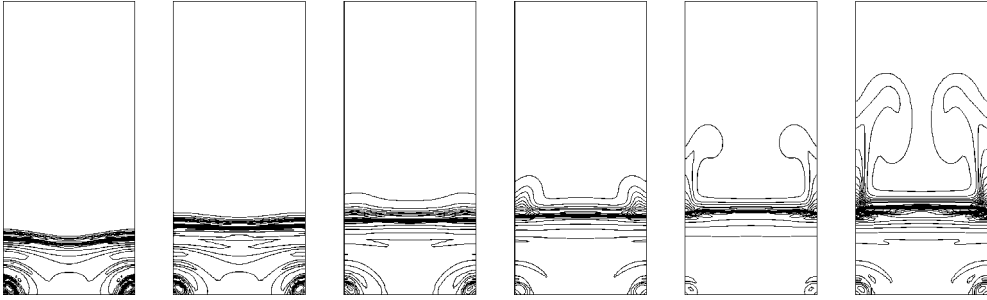


Fig. 9. Evolution of the mass fraction field for successive steps of growth, $Ra_s = 80$.

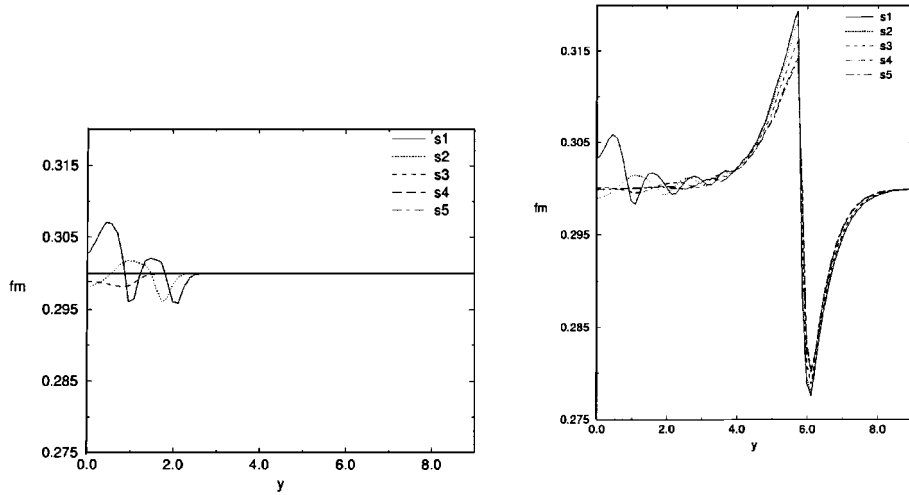


Fig. 10. Evolution of the mass fraction (f_m noted C in the text) function of the y coordinate in five positions ($z = s_i$, $i = 1, \dots, 5$) for the first (left) and last step of growth (right), $Ra_s = 10$.

number $Ra_s = 41$. The comparison for both models shows that the maximum values of the convective intensity are comparable for high values of Rayleigh number. Because of the displacement of the interface the boundary layer induced by the mass fraction gradient is weaker in this case.

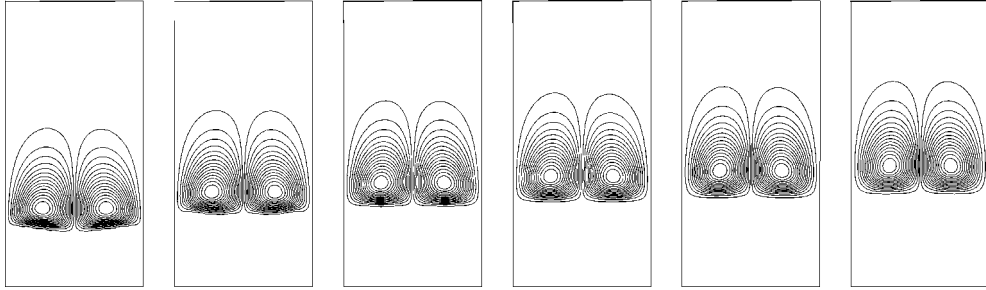


Fig. 11. Evolution of hydrodynamic field, $Ra_s = 10$.

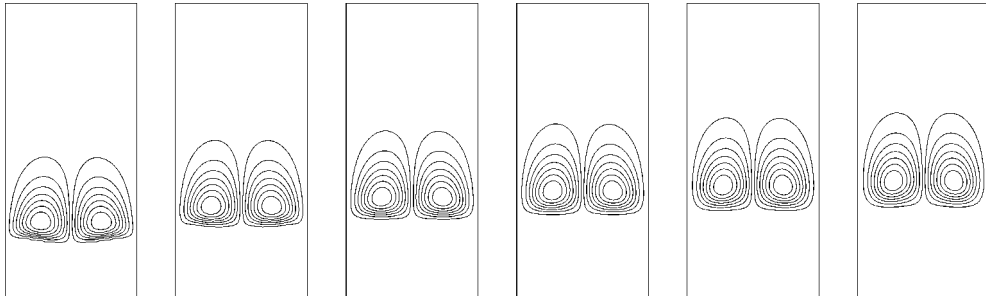


Fig. 12. Evolution of hydrodynamic field, $Ra_s = 20$.

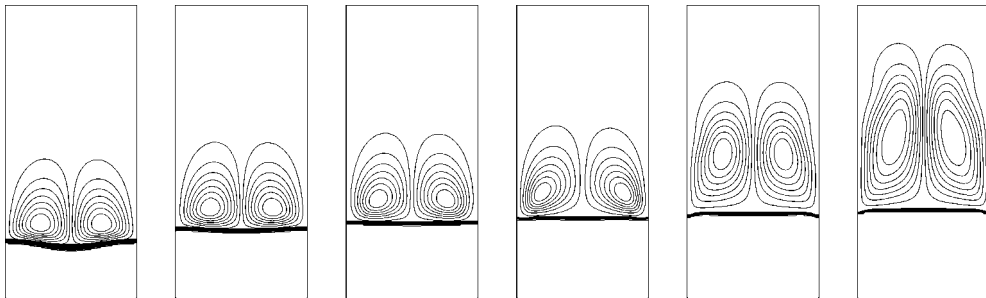


Fig. 13. Evolution of hydrodynamic field and the solid/liquid interface, $Ra_s = 80$.

This configuration limits the effects of convective transport on the solute field, which explains the less disturbed structure of this field (Figs. 7–9).

Taking into account the effects of thermal Rayleigh number $Ra_t = 500$. The convective motion develops with a symmetric regime but shows an increase of the stream-function maximum value. The development begins with four cells, two lower ones near the interface are due to the solutal convection and the higher cells are due to the radial thermal gradients established within the top of the adiabatic zone as seen on the temperature field (Fig. 6). After the first step the higher and lower cells give one convective cell occupying all the fluid phase (Figs. 14 and 15).

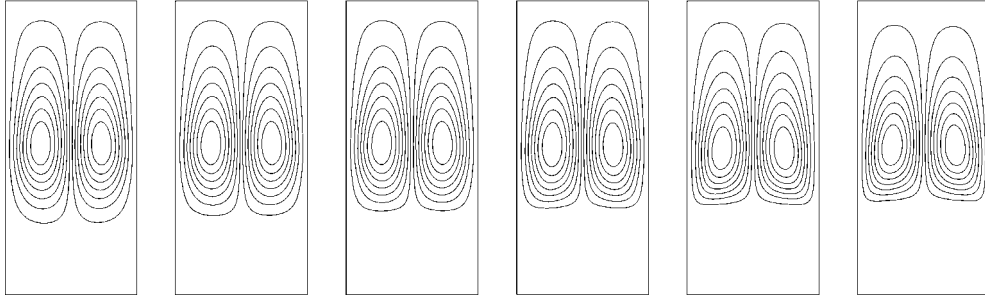


Fig. 14. Evolution of the streamlines for both thermal and solutal convection $Ra_s = 80$ and $Ra_t = 500$.

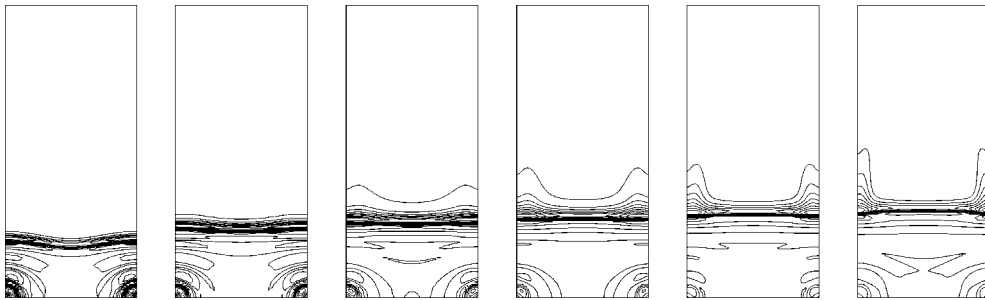


Fig. 15. Evolution of the mass fraction field for both thermal and solutal convection, $Ra_s = 80$ and $Ra_t = 500$.

5. Conclusion

A numerical investigation is proposed for 2D convective flow developing in the liquid phase above an alloy directional growing in the vertical Bridgman configuration. The homogeneous formulation of Navier–Stokes, energy and species conservation permits to consider extended model accounting solid/liquid phase change without writing explicitly the transmission conditions at the phase change interface.

By understanding the extension of CFD methods to fluid flow calculations under the phase transition conditions a first step of better physical interpretation of this complex phenomena is taken. Crystal growers are concerned with the interaction of convective phenomena with the growth interface. An important aspect regarding thermal convection in directional solidification configuration is achieved.

The extension to solutal convection for binary alloy makes an important advance to realistic growth model. The work presented in this paper gives a first step in this way. It is be shown that the method is able to describe with accuracy close to spectral one complex phenomena occurring inreduced configuration to fluid phase. The global model with solid phase accounts correctly the interface displacement and its interaction with solutal field. A weak coupling is considered in this study. For the continuation of this work a strong coupling must be studied to extend these solutal results to similar ones shown in El Ganaoui thesis [15] involving strong interaction between solidification front and solid/liquid interface under thermal convection carried out for pure material.

Acknowledgements

We would like to thank Professor P. Haldenwang from laboratory LMSNM of CNRS for helpful and discussions. We thank also the CNRS for support on CRAY C98 by conseil scientifique of IDRIS center of Orsay. Support from french space agency CNES are also acknowledged.

References

- [1] Fletcher CAJ. Computational techniques for fluid dynamics. Berlin: Springer; 1988.
- [2] Peyret R, Taylor TD. Computational methods for fluid flow. New York: Springer; 1983.
- [3] Luquin B, Pironneau O. Introduction au calcul scientifique. Paris: Masson; 1996.
- [4] Carslaw HS, Jaeger JC. Conduction of heats in solids. Cambridge: Cambridge University Press; 1959.
- [5] Flemmings MC. Solidification processing. New York: McGraw-Hill; 1974.
- [6] Brisson O, El Ganaoui M, Simmonet V, Launay JC. Experimental determination of physical parameters of AgGaS₂ crystal and numerical and experimental analysis of the Bridgman–Stockbarger solidification for the growth of crystal in ampoule with conical shape. *J Cryst Growth* 1999;204:201–12.
- [7] Simpson JE, de Groh III HC, Garimella SV. Directional solidification of pure succinonitrile and a succinonitrile–acetone alloy. NASA/TM-1999-209381, August 1999.
- [8] Crank IJ. Free and moving boundary problems. Oxford, UK: Clarendon Press; 1984.
- [9] Landau HG. Heat conduction in melting solid. *Quart Appl Math* 1959;8(1):81–94.
- [10] Voller VR, Prakash C. A fixed grid numerical modelling methodology for convection diffusion mushy region phase change problems. *Int J Heat Mass Transf* 1987;30(8):1709–19.
- [11] Bennon WD, Incropera FP. A continuum model for momentum, heat and species transport in binary solid–liquid phase change systems: 1. Model formulation. *Int J Heat Mass Transf* 1987;30(10):2161–70.
- [12] Voller VR, Cross M. Accurate solutions of moving boundary problems using the enthalpy method. *Int J Heat Mass Transf* 1980;24:545–56.
- [13] Le Marec C, Guérin R, Haldenwang P. Pattern study in 2D solutal convection above a Bridgman-type solidification front. *Phys Fluids* 1997;9(11):3149.
- [14] Le Marec C. Etude numérique de l'influence de la convection thermosolutale sur la solidification dirigée d'un alliage binaire dans un creuset cylindrique. Thèse de l'Université d'Aix-Marseille. 1996.
- [15] El Ganaoui M. Modélisation numérique de la convection thermique instationnaire en présence d'un front de solidification déformable. Thèse de l'Université d'Aix-Marseille, Octobre 1997.
- [16] Guérin RZ, Billia B, Haldenwang P, Roux B. Solutal convection during directional solidification of a binary alloy: influence of side walls. *Phys Fluids* 1988;31:2086.
- [17] Rappaz M. Modelling of microstructure formation in solidification processes. *Int Mater Rev* 1989;34:93–123.
- [18] Eymard R, Gallouet Th, Herbin R. Finite volume methods. In: Ciarlet PG, Lions JL, editors. Handbook of numerical analysis. New York: North-Holland; 1999, preprint in press.
- [19] Huppert EH. The fluid mechanics of solidification. *J Fluid Mech* 1990;212:209–40.
- [20] Le Quéré P, Alziary de Roquefort T. Computation of natural convection in 2D cavity with Chebyshev polynomials. *J Comput Phys* 1985;57:210.
- [21] Larroude Ph, Ouazzani J, Alexander JID, Bontoux P. Symmetry breaking flow transitions and oscillatory flows in 2D directional solidification model. *Eur J Mech B/Fluids* 1994;13(3):353.
- [22] Angot Ph, Caltagirone JP. Natural convection through periodic porous media. In: 9th Int Heat Transfer Conf Jerusalem, vol. 5. New York: Hemisphere; 1990, p. 219–24.
- [23] Angot Ph. Analysis of singular perturbations on the Brinkman problem for fictitious domain models of viscous flows. *Math Meth Appl Sci* 1999;22:1395–412.
- [24] Brown RA. Theory of transport processes in single crystal growth from the melt: a review. *AICHE J* 1988;34: 881–911.

- [25] El Ganaoui M, Mazhorova OS, Bontoux P. Computer simulation of pure and alloys melt growth. *Microgravity Quart Rev* 2000;7(4):171–8.
- [26] Chang J, Brown RA. Radial segregation induced by natural convection and melt–solid interface shape in vertical Bridgman growth. *J Crystal Growth* 1983;63:343–64.
- [27] Morvan D, El Ganaoui M, Bonotoux P. Numerical simulation of 2D crystal growth problems in a vertical Bridgman–Stockbarger furnace, latent heat effects and crystal-melt in interface morphology. *Int J Heat Mass Transf* 1999;42:573–9.
- [28] El Ganaoui M, Bontoux P, Morvan D. Localisation d’un front de solidification en interaction avec un bain fondu instationnaire. Paris: CR Acad Sciences; 1999. p. 41–8, t. 327, Série II b.
- [29] Lamazouade A, El Ganaoui M, Morvan D, Bontoux P. Simulation numérique par une approche porosité enthalpie de la convection thermique et solutale dans une ampoule de Bridgman. *Int J Therm Sci* 1999;8(38):674–83.
- [30] Timchenko V, El Ganaoui M, Leonardi E, Bontoux P, de Vahl Davis G. Effects of thermal conductivities on heat and mass transfer during directional solidification. *Proceeding European Science Foundation, Applied Mathematics for Industrial Flow Problems*. Warsaw, Poland, 24–26 July, 1999. p. 151–4.
- [31] McFadden GB, Coreill SR, Boivert RF. *Phys Fluids* 1985;28:2716.
- [32] Impey MD, Riley DS, Wheeler AA, Winters KH. Bifurcation analysis of solutal convection during directional solidification. *Phys Fluids A* 1991;3:535.
- [33] Leonard BP, Mokhtari S. Beyond first-order upwinding the ultra-sharp alternative for nonoscillatory steady state simulation of convection. *Int J Numer Meth Engng* 1990;30:729–66.
- [34] Droll P, El Ganaoui M, Kadinski L, et al. High performance computer codes and their application to optimize crystal growth processes I. In: *Numerical flow simulation I. Notes on numerical fluid mechanics*, vol. 66. Braunschweig: Vieweg Verlag; 1998, p. 115–43.
- [35] Timchenko V, Chen PYP, de Vahl Davis G, Leonardi E, de Groh III HC. Directional solidification in microgravity. *Heat Transfer* 1998:241–6.
- [36] Lamazouade A. Modélisation de la convection solutale lors de procédés de Bridgman–Stockbarger par une méthode enthalpique. Thèse de l’Université d’Aix-Marseille, Juin 2000.